Deformed shell effects in ^{48}Ca + ^{249}Bk quasifission fragments

K. Godbey* and A. S. Umar†
Department of Physics and Astronomy, Vanderbilt University, Nashville, Tennessee 37235, USA

C. Simenel‡
Department of Theoretical Physics and Department of Nuclear Physics, Research School of Physics and Engineering, The Australian National University, Canberra ACT 2601, Australia

(Received 18 June 2019; published 12 August 2019)

Background: Quasifission is the main reaction channel hindering the formation of superheavy nuclei (SHN). Its understanding will help to optimize entrance channels for SHN studies. Quasifission also provides a probe to understand the influence of shell effects in the formation of the fragments.
Purpose: Investigate the role of shell effects in quasifission and their interplay with the orientation of the deformed target in the entrance channel.
Methods: ^{48}Ca + ^{249}Bk collisions are studied with the time-dependent Hartree-Fock approach for a range of angular momenta and orientations.
Results: Unlike similar reactions with a ^{238}U target, no significant shell effects which could be attributed to the ^{208}Pb "doubly magic" nucleus are found. However, the octupole deformed shell gap at $N = 56$ seems to strongly influence quasifission in the most-central collisions.
Conclusions: Shell effects similar to those observed in fission affect the formation of quasifission fragments. Mass-angle correlations could be used to experimentally isolate the fragments influenced by $N = 56$ octupole shell gaps.

DOI: 10.1103/PhysRevC.100.024610

I. INTRODUCTION

Quasifission occurs when the collision of two heavy nuclei produces two fragments with similar characteristics to fusion-fission fragments, but without the intermediate formation of a fully equilibrated compound nucleus [1–4]. It is the main mechanism that hinders fusion of heavy nuclei and consequently the formation of superheavy elements [5–10]. It is thus crucial to achieve a deeper insight of quasifission in order to minimize its impact and maximize the formation of compound nuclei for heavy and superheavy nuclei searches.

Quasifission also provides a unique probe to quantum many-body dynamics of out-of-equilibrium nuclear systems. For instance, quasifission studies bring information on mass equilibration timescales [11–13], on shell effects in the exit channels [14–18], as well as on the nuclear equation of state [19,20]. In fusion-fission, the exit channel is essentially determined by the properties of the compound nucleus and does not depend *a priori* on the specificity of the entrance channel. This is not the case in quasifission, which is known to preserve a strong memory of the entrance channel properties. As a result, understanding the interplay between the entrance and exit channels requires a significant amount of experimental systematic studies. These include investigations of the role of beam energy [15,21,22], dissipation [23], fissility of the compound nucleus [24,25], deformation of the target [15,26–29], spherical shells of the collision partners [30,31], and the neutron-to-proton ratio N/Z of the compound nucleus [32,33].

On the theory side, quasifission has been studied with various approaches. This includes classical methods such as a transport model [34], the dinuclear system model [35–38], and models based on the Langevin equation [39–43]. Microscopic approaches such as quantum molecular dynamics [44–46] and the time-dependent Hartree-Fock (TDHF) theory [17,18,32,43,47–57] have also been used. See Refs. [58–61] for recent reviews on TDHF.

An advantage of microscopic calculations is that their only inputs are the parameters of the energy density functional describing the interaction between the nucleons. Since these parameters are usually fit to nuclear structure properties only, such calculations do not require additional parameters determined from reaction mechanisms, such as nucleus-nucleus potentials. In addition, TDHF calculations treat both reaction mechanisms and structure properties on the same footing. This is important for reactions with actinide targets which exhibit a strong quadrupole deformation.

Indeed, the outcome of the calculations strongly depend on the orientation of the nuclei. For instance, TDHF calculations of the ^{40}Ca + ^{238}U reaction showed that only collisions with the side of the ^{238}U could lead to configurations which are compact enough to enable fusion [17]. This is contrary to the collisions with the tip of ^{238}U which seem to always lead to a fast quasifission [after ∼5–10 zeptoseconds (zs) of contact

*kyle.s.godbey@vanderbilt.edu
†umar@compsci.cas.vanderbilt.edu
‡cedric.simenel@anu.edu.au

 ©2019 American Physical Society

time] as long as contact between collision partners is achieved. A remarkable observation of this work was the systematic production of lead nuclei ($Z = 82$), known to possess a strong spherical proton shell gap, in tip collisions only, showing a strong influence of orientation-dependent shell effects in the production of the fragments. Such influence of shell effects was proposed to explain peaks in fragment mass distributions [14,15,17], but experimental confirmation came only recently with the observation of a peak of quasifission fragments at $Z = 82$ protons from x-ray measurements [18].

Deformed shell effects in the region of ^{100}Zr have also been invoked to interpret the outcome of TDHF simulations of ^{40,48}Ca + ^{238}U, ^{249}Bk collisions [49,51]. It is then natural to wonder if other shell effects, spherical or deformed, could be driving the dinuclear system out of its compact shape, into quasifission. Potential candidates are shell effects known to influence the outcome of fission reactions. It has recently been proposed that octupole deformed shell effects, in particular with Z or $N = 52$–56, are the main driver to asymmetric fission [62,63]. The fact that ^{208}Pb can easily acquire an octupole deformation (its first-excited state is a 3^- octupole vibration) is compatible with this interpretation. Note also that some superheavy nuclei like ^{294}Og are expected to encounter superasymmetric fission and produce a heavy fragment around ^{208}Pb [64–67], confronting the idea that quasifission valleys could match fission ones.

In this work we study the ^{48}Ca + ^{249}Bk reaction with the TDHF approach. The choice of this reaction is motivated by its success in forming the element $Z = 117$ [68–72]. Previous TDHF studies of quasifission with actinide targets were restricted to one or two orientations of the target to limit computational time. However, to allow possible comparison with experimental data, it is important to simulate a range of orientations in addition to the usual tip and side configurations. We therefore performed systematic simulations, spanning both a range of orientations and a range of angular momenta. This allows us to study correlations between, e.g., mass, angle, kinetic energy, as well as to predict distributions of neutron and proton numbers at the mean-field level. These distributions are used to identify potential shell gaps driving quasifission. The method is described in Sec. II. The results are discussed in Sec. III. We then conclude in Sec. IV.

II. METHOD

The TDHF theory provides a microscopic approach to investigate a large selection of phenomena observed in low-energy nuclear physics [58,59,73]. In particular, TDHF provides a dynamic quantum many-body description of nuclear reactions in the vicinity of the Coulomb barrier, such as fusion [74–89], deep-inelastic reactions and transfer [60,77,90–97], and dynamics of (quasi)fission fragments [17,49–52,80,98–102]. The classification of various reaction types in TDHF is done by calculating the time evolution of expectation values of one-body observables: fragments' centers of masses, mass and charges on each side of the neck, kinetic energy, and orbital angular momentum, among others. Quasifission is characterized by two final-state fragments that emerge after a long-lived composite system (typically longer than 5 zs) and final fragment masses $A_f = A_{\rm CN}/2 \pm 20$ or more. In addition, final TKEs distinguish quasifission from highly damped deep-inelastic collisions, which have a smaller mass and charge difference between initial and final fragments. In TDHF the mass and charge difference between the initial nuclei and the final fragments measure the number of nucleons transferred. As discussed above, fusion corresponds to the case where the final product remains as a single composite for a reasonably long time, chosen here to be 35 zs.

The TDHF equations for the single-particle wave functions,

$$h(\{\phi_\mu\})\phi_\lambda(r,t) = i\hbar\frac{\partial}{\partial t}\phi_\lambda(r,t)\ (\lambda = 1,\ldots,A), \qquad (1)$$

can be derived from a variational principle. The main approximation in TDHF is that the many-body wave function $\Phi(t)$ is assumed to be a single time-dependent Slater determinant at all times. It describes the time-evolution of the single-particle wave functions in a mean-field corresponding to the dominant reaction channel. During the past decade it has become numerically feasible to perform TDHF calculations on a three-dimensional (3D) Cartesian grid without any symmetry restrictions and with much more accurate numerical methods [93,103–105].

In this paper, we focus on fusion and quasifission in the reaction ^{48}Ca + ^{249}Bk. In our TDHF calculations we use the Skyrme SLy4d energy density functionals [106], including all of the relevant time-odd terms in the mean-field Hamiltonian. Static Hartree-Fock (HF) calculations without pairing predict a spherical density distribution for ^{48}Ca while ^{249}Bk shows prolate quadrupole and hexadecupole deformation, in agreement with experimental observations. Numerically, we proceed as follows: First we generate very-well-converged static HF wave functions for the two nuclei on the 3D grid. Three-dimensional TDHF initialization of the deformed ^{249}Bk nucleus, with a particular alignment of its symmetry axis with respect to the collision axis, can be most easily achieved by evaluating the initial guess for HF calculations on mesh values rotated with respect to the code axes. Subsequent HF iterations do not change this orientation, thus resulting in the desired HF solution. This procedure involves no interpolation procedure and is the most straightforward method to implement in TDHF codes [107]. Otherwise, static solutions obtained for extreme angles (0° or 90° with respect to collision axis) can be very accurately interpolated to arbitrary angles [107] followed by a few additional static iterations for extra accuracy.

The initial separation is chosen to be 30 fm with nuclei in their ground states. The nuclei are assumed to arrive to this separation on a Coulomb trajectory for the purpose of initializing the proper boosts. In the second step, we apply a boost operator to the single-particle wave functions. The calculations end when the fragments are well separated (or after 35 zs if they are still in contact). Outgoing Coulomb trajectories are then assumed to determine the scattering angle.

The time-propagation is carried out by using a Taylor series expansion (up to orders 10–12) of the unitary mean-field propagator, with a time step $\Delta t = 0.4$ fm/c. For reactions leading to superheavy dinuclear systems, the TDHF

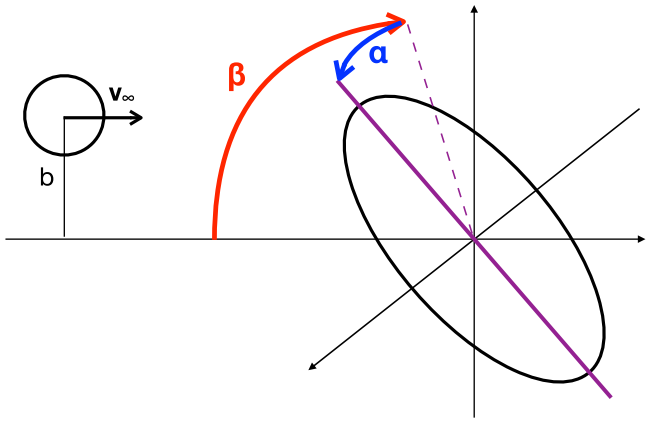

FIG. 1. Schematic representation of the initial configuration for an impact parameter b and a velocity vector $\mathbf{v}_\infty$ defining the collision plane and the collision axis. The orientation of the target is defined by the angles β (rotation around the axis perpendicular to the reaction plane) and α (rotation around the collision axis).

calculations require very long CPU times: a single TDHF run at fixed $E_{\text{c.m.}}$ energy for a fixed impact parameter b and orientation angle β takes about 2–3 days of CPU time on a 16-processor LINUX workstation.

Assuming the ^{249}Bk nucleus to be axially symmetric with no octupole deformation, the cross section or yield for a specific reaction channel ξ is proportional to

$$\sigma_\xi \propto \sum_L (2L+1) \int_0^{\frac{\pi}{2}} d\beta \sin\beta \int_0^{\pi} d\alpha P_L^{(\xi)}(\beta,\alpha). \qquad (2)$$

Here, $P_L^{(\xi)}(\beta,\alpha)$ is the probability for the reaction channel ξ and an orientation of the target defined by the rotation angles β and α (see Fig. 1). The orientation of the deformation axis is obtained by applying first a rotation by an angle β around the axis perpendicular to the reaction plane, and then a rotation by an angle α around the collision axis.

The TDHF calculations are performed for a range of orbital angular momenta $L_i\hbar$ with $\{L_i\} = \{0, 10, 20, \ldots, N_L\}$ and $N_L = 12$ or 13, depending on the orientation (some orientations lead to quasi-elastic collisions at $L = 120$, in which case $L = 130$ is not computed). The first term is then replaced by

$$\sum_L (2L+1) \rightarrow \sum_{i=1}^{N_L} K_i \quad \text{with} \quad K_i = \sum_{L=L_i-\Delta_i^-}^{L_i+\Delta^+} (2L+1),$$

where $\Delta^+ = 5$, $\Delta_1^- = 0$, and $\Delta_{i\neq 1} = 4$.

The double integral in Eq. (2) is computationally too demanding. The integral over α is then replaced by a sum over probabilities for $\alpha = 0$ and π. Equivalently, we can ignore α and extend the integral over β up to π. We then define the probability

$$\tilde{P}_{L_i}^{(\xi)}(\beta) = \begin{cases} P_{L_i}^{(\xi)}(\beta, 0) & \text{if } \beta \leqslant \frac{\pi}{2} \\ P_{L_i}^{(\xi)}(\pi-\beta, \pi) & \text{if } \beta > \frac{\pi}{2}. \end{cases}$$

The remaining integral over β is discretized with $N_\beta = 12$ angles $\{\beta_n\} = \{0^\circ, 15^\circ, 30^\circ, \ldots, 165^\circ\}$. We can finally write

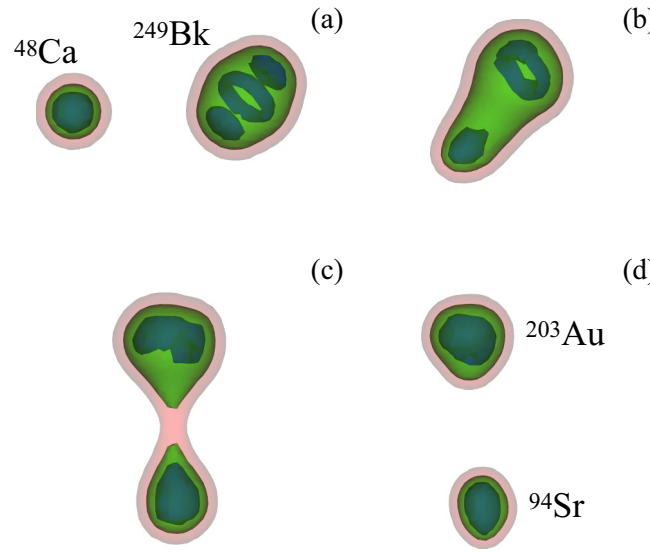

FIG. 2. Isodensity surfaces at $\rho = 0.145$, 0.1, and 0.02 fm^{-3} in blue, green, and pink, respectively, shown at times (a) $t \simeq 0$, (b) 2.1, (c) 5.8, and (d) 6.4 zs for an initial orientation $\beta = 135^\circ$ and an angular momentum $L = 60\hbar$. For visualization purposes, the reaction plane is 37° off the plane of the page.

the approximate cross section as

$$\sigma_\xi \simeq \sum_{i=1}^{N_L} K_i \sum_{n=1}^{N_\beta} C_n \tilde{P}_{L_i}^{(\xi)}(\beta_n), \qquad (3)$$

where we have defined

$$C_n = \begin{cases} 2(1-\cos\delta) & \text{if } n = 1 \\ \cos(\beta_n - \delta) - \cos(\beta_n + \delta) & \text{if } n > 1, \end{cases}$$

with $\delta = 7.5^\circ$. Note that, because of its semiclassical behavior, the TDHF theory leads to probabilities $\tilde{P}_{L_i}^{(\xi)}(\beta_n) = 0$ or 1 for the reaction channel ξ for a given orientation and angular momentum.

III. RESULTS

The ^{48}Ca + ^{249}Bk at $E_{\text{c.m.}} = 234$ MeV has been studied as a function of the orientation β of the target (see Fig. 1) and as a function of orbital angular momentum L, given in units of $\hbar$, totaling 148 collisions.

A. Quasifission characteristics

Figure 2 shows a typical example of density evolution for a noncentral collision. Different isodensity surfaces are represented. The rings observed at highest density in Figs. 2(a) and 2(b) are coming from shell-structure effects [58]. After contact, the nuclei are trapped in a potential pocket, forming a dinuclear system [Fig. 2(b)] which, unlike in fusion, does not reach an equilibrated compound nucleus. When the dinuclear system fissions [Fig. 2(c)], it forms two fragments [Fig. 2(d)], which preserve a memory of the entrance channel.

The outgoing fragments for this reaction are ^{94}Sr and ^{203}Au. Such a significant mass transfer towards a more mass-symmetric configuration is one of the characteristics

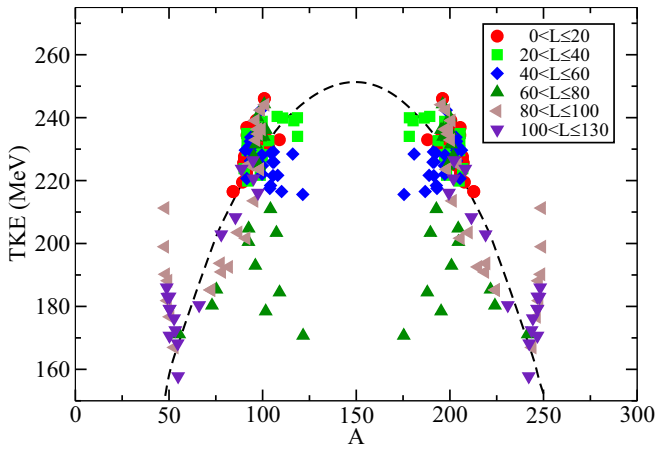

FIG. 3. Total kinetic energy of the fragments as a function of their mass ratio. The curve corresponds to the Viola systematics [108,109].

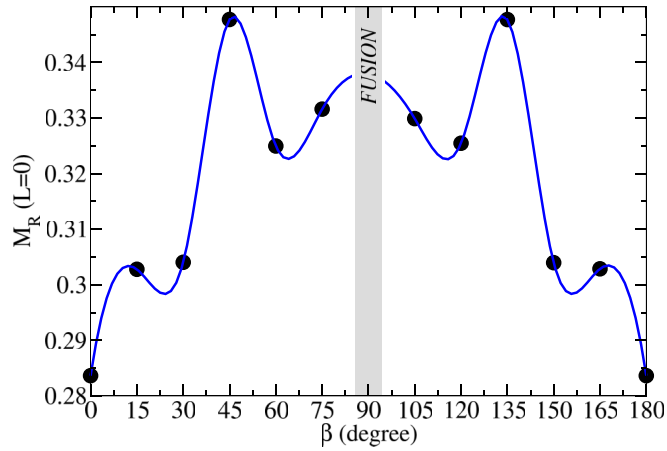

FIG. 4. Mass ratio M_R as a function of orientation angle β for central collisions. Fusion is indicated by the shaded area.

of quasifission. A second characteristic is the rotation of the dinuclear system before scission. This rotation is due to the initial angular momentum for noncentral collisions. For contact times $\tau < 20$ zs, the dinuclear system usually does not undergo a full rotation before scission, resulting in so-called fast quasifission [25,110]. Such times are also too short for the system to achieve full mass equilibration, so two fragments form with similar masses. Fast quasifission then results in correlations between masses and angles, which can be used to infer the timescale of the reaction [11,13]. The density evolution represented in Fig. 2 is an example of a fast quasifission reaction because the fragments are in contact for ∼6 zs and the dinuclear system rotates by only ∼90 degrees. In fact, all quasifissions observed in our calculations for this system correspond to fast quasifission, producing fragment mass-angle correlations, which will be studied in Sec. III C.

Another characteristic of quasifission is that the reaction is fully damped. In quasifission, the outgoing fragments have a total kinetic energy (TKE) essentially determined by their Coulomb repulsion at scission. As a first approximation, this TKE does not depend on the beam energy. Figure 3 shows the mass-energy distribution (MED), i.e., the distribution of TKE as a function of the number of nucleons A in the fragments. Except for quasi-elastic reactions in which the masses of the fragments are very close to the projectile and target masses, the TKE are generally distributed around the Viola systematics [108,109] (dashed line), which gives an empirical estimate of fully damped fission fragments.

Each color in Fig. 3 shows the location in the MED that is expected for a given range of orbital angular momenta. In each case, two or three values of L and thirteen angles β are included. The more-central collisions ($L \leqslant 80\hbar$) all lead to quasifission, while more-peripheral collisions ($L > 80\hbar$) lead to both quasielastic and quasifission reactions. This indicates a strong influence of orientation on the reaction outcome.

B. Effect of target orientation in central collisions

Different orientations of the target lead to different compactness of the dinuclear system. A clear relation between orientation and compactness is obtained in the case of central collisions ($L = 0$), in which case less-compact configurations are obtained for $\beta = 0$ and 180 degrees, leading to collisions with the tips of the target, while the most-compact configurations are obtained for $\beta = 90$ degrees, leading to collisions with the side. For noncentral collisions, the relationship between orientation and compactness is less straightforward and can be estimated assuming Coulomb trajectories until the distance of closest approach [17].

Figure 4 shows the mass ratio of the fragments, defined as the ratio between the mass of the fragment and the total mass of the system, as a function of the orientation for central collisions. A slight asymmetry between β and $\pi - \beta$ is observed due to a small violation of symmetry under reflection across the plane orthogonal to the main deformation axis of ^{249}Bk HF ground state.

Fusion is only observed for side collisions, in agreement with previous TDHF studies [17,49,51]. Overall, a small increase of the mass ratio from $M_R \approx 0.28$ to 0.35 is observed when going from tip orientations to more-compact configurations. There is, however, no clear transition associated with an eventual critical angle β_{crit} when going from tip to side orientation in this system (except for when fusion is achieved). This shows the importance of considering a full range of intermediate orientations in order to realize quantitative predictions.

C. Correlations between fragment masses and scattering angles

Experimental studies of correlations between fragment masses and scattering angles have led to considerable insights into quasifission mechanisms in the past [11,12,17,18,25,29–32,110]. TDHF calculations have been used recently to help interpret qualitatively these correlations [17,32,51,52]. However, these theoretical studies were somewhat limited by the restriction of initial orientations.

The mass-angle distribution (MAD) of the fragments is shown in Fig. 5(a). The horizontal axis gives the mass ratio $M_R = \frac{m_1}{m_1+m_2}$ where m_1 and m_2 are the masses of the fragments. These masses are for primary fragments, i.e., before

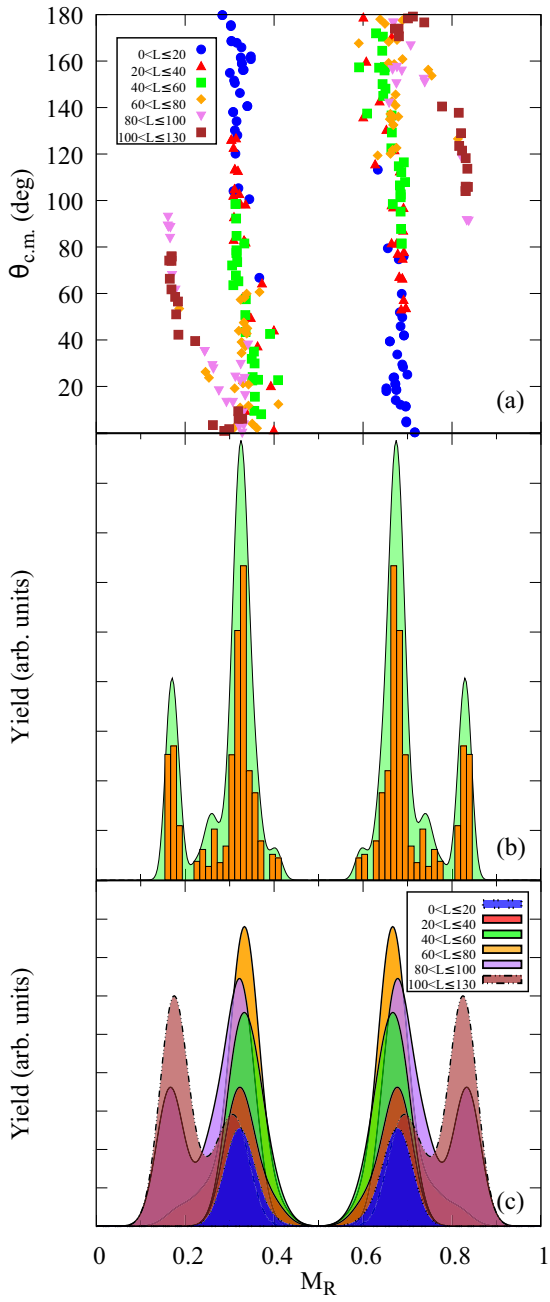

FIG. 5. (a) Distribution of scattering angle $\theta_{\rm c.m.}$ versus mass ratio M_R (MAD). The colors correspond to different ranges of angular momenta. (b) Fragment mass yield (histogram). The solid line gives a smooth representation of the histogram using the kernel density estimation with bandwidth 0.012. (c) Mass yields obtained for different ranges of angular momenta.

nucleon emission takes place. This is also what is measured experimentally using two-body kinematics techniques [11,27]. The colors represent different angular-momentum ranges, as in Fig. 3.

Most calculations lead to quasifission with fragment mass ratios $0.28 < M_R < 0.72$, while projectile and target mass ratios are at $M_R \simeq 0.16$ and 0.84, respectively. This indicates significant mass transfer towards more symmetric mass repartitions. However, full symmetry is never achieved in these TDHF calculations, unlike in ^{40}Ca + ^{238}U [17]. Most peripheral collisions with $L \geqslant 70\hbar$ lead to larger mass asymmetries and a transition from quasifission to deep-inelastic and quasi-elastic reactions. Note that fragments from elastic scattering are not shown.

We also see that quasifission fragments are distributed among the full range of scattering angles, from $\theta_{\rm c.m.} = 0$ (forward angles) to 180 degrees (backward angles). This wide angular distribution motivates the development of detectors with larger angular acceptance [9,10]. Note that each angular-momentum range leads itself to a broad distribution of angles. For instance, results from $L \leqslant 20\hbar$ are found all the way from backward angles to $\theta_{\rm c.m.} \simeq 70$ degrees, while $L \leqslant 40\hbar$ spans all angles. This is a manifestation of the impact of orientation on the angular distribution: for a given angular momentum, the scattering angle strongly depends on the orientation of the target. However, there is much less dependence of the mass on the orientation, because each orientation leads to an approximately similar mass ratio for quasifission outcomes in this system.

Interestingly, the correlation between quasifission fragment masses and angles shows a narrow mass distribution for the light fragment around $M_R \simeq 0.3$ at more backward angles with $\theta_{\rm c.m.} > 70$ degrees. At more forward angles ($\theta_{\rm c.m.} < 70$ degrees), the light fragment mass distribution broadens and slightly shifts towards larger masses ($M_R \sim 0.34$). For symmetry reasons, a similar narrow (broad) mass distribution is found in the heavy fragment at $M_R \simeq 0.7$ ($M_R \sim 0.66$) for $\theta_{\rm c.m.} < 110$ ($\theta_{\rm c.m.} > 110$) degrees. The origin of these features will be discussed using neutron and proton distributions in Sec. III E.

D. Fragment mass distributions

The theoretical MAD in Fig. 5(a) is useful to investigate correlations between mass and angle. However, it is not directly related to yields and cross sections because it does not account for the $2L + 1$ and $\sin\beta$ terms in Eq. (2). Yields are better represented in one-dimensional spectra. Figure 5(b) shows a histogram of the mass ratio yield obtained from Eq. (2). The solid line curve gives a smooth representation of the histogram. As these are more illustrative, we will only use these smooth representations of yields in later figures.

The quasifission mass yields in Fig. 5(b) are strongly peaked at $M_R \sim 0.33$ and 0.67, with a full width half maximum (FWHM) $\simeq$0.1 corresponding to a standard deviation $\sigma_{M_R} \simeq 0.042$. Note that the present TDHF calculations neglect mass distributions associated with each single TDHF calculation outcome. The latter can be computed by using particle-number projection techniques [91,93,94,111]. However, the width of the resulting distributions are known to be underestimated in dissipative collisions [112]. Beyond mean-field calculations incorporating one-body fluctuations could also be used [23,55,92,113–117]. However, these approaches are not used here because they would significantly increase computing time and would become prohibitive with large ranges of orientations and angular momenta.

We can nevertheless attempt a comparison with typical experimental mass width for quasifission distributions, keeping in mind that our theoretical prediction is a lower bound. The experimental spread σ_{M_R} can roughly be parametrized as a linear function from $\sigma_{M_R}^{(\mathrm{DIC})} \approx 0.025$, which is typical for deep-inelastic collisions (DIC) at the mass ratio of the projectile and target, to $\sigma_{M_R}^{(FF)} = 0.07$ in fusion-fission at $M_R = 0.5$ [13]. We then get an estimate of $\sigma_{M_R}^{(QF)} \approx 0.047$ at $M_R = 0.33$, which is only ∼10% higher than the TDHF prediction. The present calculations, to a large extent, account for the expected fluctuations of the mass of the quasifission fragments. These fluctuations are essentially coming from the various orientations of the deformed target nucleus.

Figure 5(c) shows the expected mass ratio yield distributions for various ranges of angular momenta L. The purpose of this figure is to compare quantitatively the relative contributions to the yields when going from central to peripheral collisions. For instance, we see that, because of the $2L + 1$ weighting factor in Eq. (2), the most-central collisions with $L \leqslant 20\hbar$, which are found at backward angles in Fig. 5(a), have also the smallest contribution to the total yield. To understand the transition from $M_R \simeq 0.30$ to 0.34 discussed at the end of Sec. III C, it will then be necessary to fully exploit the correlations between masses and angles of the quasifission fragments.

E. Identification of shell effects in quasifission fragments

Experimental indications of the role of shell effects in the production of quasifission fragments initially came from mass-yield measurements [14,15,17]. Theoretical predictions from TDHF calculations then supported these views [17,49,51]. However, to unambiguously confirm the role of shell effects, proton or neutron numbers distributions have to be measured. Only recently this was done for quasifission for the ^{48}Ti + ^{238}U reaction using x-ray detectors to identify proton numbers in the fragments [18], thus confirming the role of $Z = 82$ "magic" shell in this reaction.

To investigate the role of potential shell effects in ^{48}Ca + ^{249}Bk quasifission, the correlations between proton and neutron numbers with scattering angles have been plotted in Figs. 6(a) and 7(a), respectively. Proton and neutron numbers yields are also shown in Figs. 6(b) and 7(b), respectively. In addition to the total yields obtained without restriction on scattering angles and nucleon numbers (orange spectra), gates on quasifission fragments have also been used [rectangles in Figs. 6(a) and 7(a)] with $\theta_{\mathrm{c.m.}} > 70$ degrees for the light fragments and $\theta_{\mathrm{c.m.}} < 110$ degrees for the heavy ones. The resulting gated spectra are shown in purple in Figs. 6(b) and 7(b).

The vertical dotted line in Fig. 6 shows the expected position of fragments affected by $Z = 82$ shell effects. The heavy fragments seem to be systematically lighter, indicating that $Z = 82$ may not play a significant role in this reaction. This is surprising because TDHF studies have shown the importance of this shell gap in quasifission for ^{40,48}Ca, ^{48}Ti + ^{238}U [17,18,49].

A similar comparison is made with the magic number $N = 126$ in Fig. 7. Here, we see that some fragments are

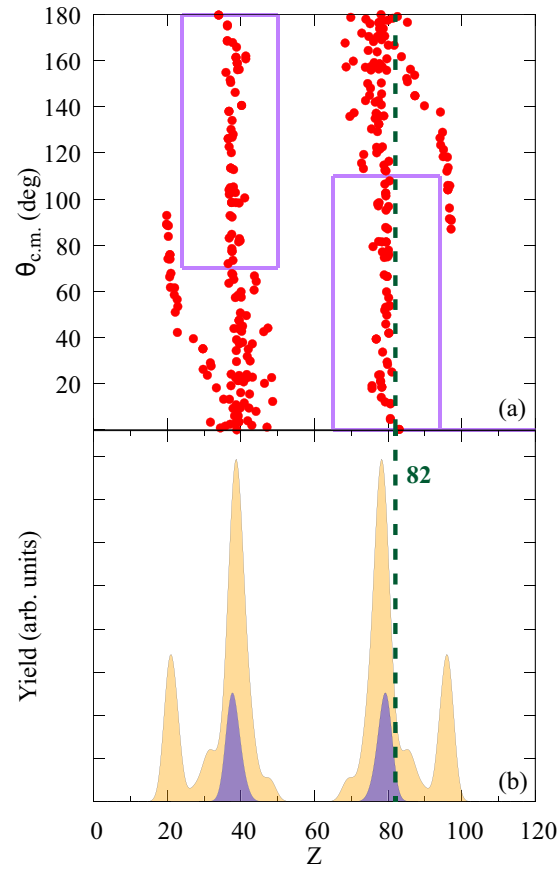

FIG. 6. (a) Distribution of scattering angle $\theta_{\mathrm{c.m.}}$ versus proton number Z (ZAD). (b) Fragment proton number yield without (lighter shade) and with angular cut $\theta_{\mathrm{c.m.}} > 70$ degrees (darker shade). The vertical line represents potential proton shell gap.

indeed formed with $N = 126$. However, both the centroids of the ungated and gated distributions are shifted towards smaller neutron numbers. For the gated spectrum, the shift is relatively small because the peak is centered at $\overline{N}_{\mathrm{gated}} \simeq 124$. Nevertheless, spherical shell effects are known to be quite localized in the nuclear chart and this "proximity" may as well be coincidental. Other spherical shell effects are also excluded for both protons and neutrons. In particular, the quasifission peaks are far from $Z = 50$ or $N = 50$.

This leaves us with potential deformed shell effects. For instance, the importance of octupole deformed shell gaps at $Z = 52$–56 [62] and $N = 52$–56 [63] have recently been shown to have an important role in driving heavy systems towards asymmetric fission. As a results of these gaps, the nuclei can easily acquire octupole deformations for a small cost (and sometimes even a gain) in energy. This is why their production as fission fragments is naturally favored, as the fissioning system has no choice but to go through a shape with a neck just before scission, imposing strong octupole deformations in the fragments. Despite its strong spherical shell effects which are expected to energetically favor its production, the formation of ^{132}Sn as a fission fragment is hindered by its strong resistance to octupole deformations. This is not the case, however, of ^{208}Pb which can easily

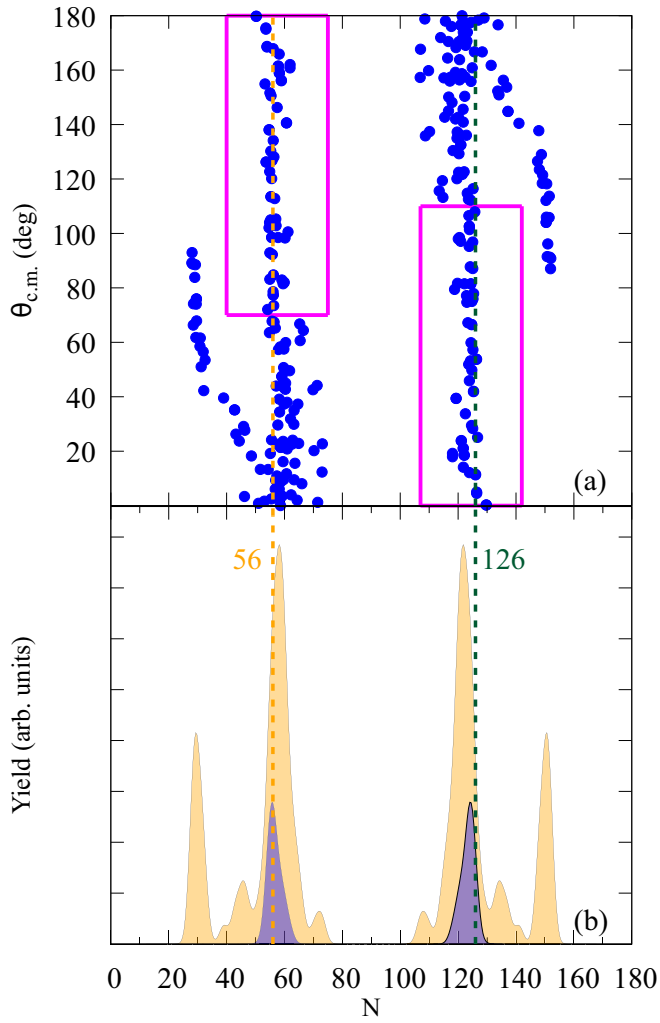

FIG. 7. (a) Distribution of scattering angle $\theta_{\text{c.m.}}$ versus neutron number N (NAD). (b) Fragment neutron number yield without (lighter shade) and with angular cut $\theta_{\text{c.m.}} > 70$ degrees (darker shade). The vertical lines represent potential neutron shell gaps.

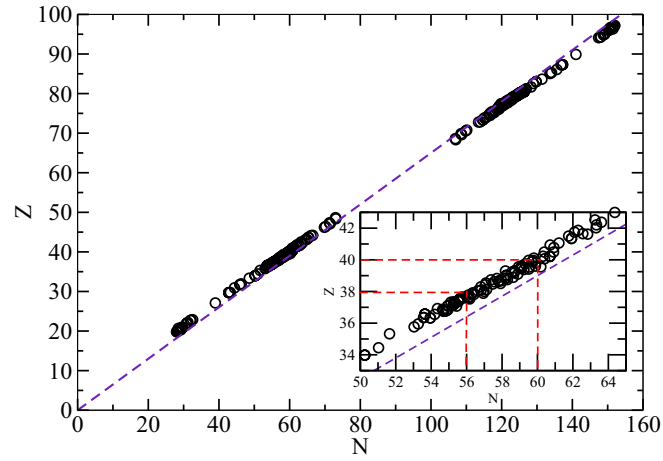

FIG. 8. Distribution of proton number Z versus neutron number N of the fragments. The dashed line represents the N/Z ratio of the compound nucleus. The inset is a zoom around the light fragment. Thin dashed lines indicate the positions of ^{94}Sr ($Z = 38$, $N = 56$) and ^{100}Zr ($Z = 40$, $N = 60$).

acquire octupole deformations thanks to its low-lying octupole 3^- state.

The orange vertical dotted line in Fig. 7 indicates the expected location of fragments affected by the $N = 56$ octupole deformed shell gap. It matches very well the position of the gated peak, providing a plausible explanation for the origin of this narrow distribution of quasifission fragments at backward angles, corresponding to more-central collisions.

As discussed in Sec. III C, however, more-peripheral collisions ($\theta_{\text{c.m.}} < 70$ degrees for the light fragment) lead to the production of slightly more symmetric quasifission fragments. For the light fragment, the Z and N distributions of these more-peripheral quasifission events [see Figs. 6(a) and 7(b)] seem to be centered around $\overline{N}_{\text{periph}} \approx 60$ and $\overline{Z}_{\text{periph}} \approx 40$, respectively, indicating the production of fragments in the ^{100}Zr region. Similar observations were already made in ^{40,48}Ca + ^{238}U systems [49].

Figure 8 shows the distribution of fragments in the N and Z plane. We see that, due to a strong symmetry energy, the fragments have N/Z ratios very close to the one of the compound nucleus. Nevertheless, the light fragments are slightly more proton rich, and the heavy fragments more proton deficient, due to the stronger Coulomb repulsion in the latter. The production of fragments in the ^{100}Zr region is confirmed in the inset of Fig. 8. We also see that the fragments with $N = 56$ neutrons correspond essentially to ^{94}Sr, as also illustrated in Fig. 2.

Shell effects are known to evolve with the deformation of the nucleus. To confirm the presence of shell effects, it is then necessary to verify that the deformation is the one expected to exhibit a shell gap. Typical isosurface densities for reactions just after scission leading to the production of a ^{100}Zr (top) and of a ^{94}Sr (bottom) fragment are shown in Fig. 9. In particular, the ^{94}Sr fragment is quite compact with a strong octupole shape, similar to what is observed in fission

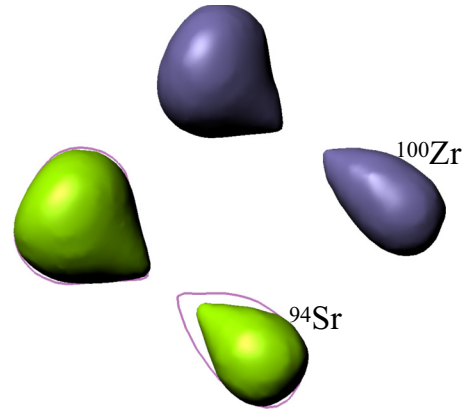

FIG. 9. Isodensity surfaces at $\rho = 0.1$ fm^{-3} for $L = 90\hbar$ and $\beta = 120^\circ$ (top), and $L = 60\hbar$ and $\beta = 135^\circ$ (bottom), just after the breaking of the neck. The light fragment (right) in the top is a ^{94}Sr ($Z = 38$, $N = 56$) and a ^{100}Zr ($Z = 40$, $N = 60$) in the bottom. The contour line in the bottom represents the same density as in the top.

of mercury isotopes producing $N = 56$ fragments to octupole shell gaps [63]. The ^{100}Zr fragment is also octupole deformed (as the density is shown just after breaking of the neck) but with a much more elongated shape. Neutron rich zirconium isotopes are indeed expected to exhibit strong quadrupole deformations [118–120].

IV. CONCLUSIONS

The ^{48}Ca + ^{249}Bk reaction, used experimentally to produce tennessine ($Z = 117$), has been studied at a center-of-mass energy of 234 MeV with time-dependent Hartree-Fock simulations. Properties of quasifission fragments, such as mass, numbers of protons and neutrons, kinetic energy, and scattering angles have been studied systematically.

Unlike previous TDHF studies of quasifission, a broad distribution of orientations of the target has been considered for the first time, allowing for the prediction of, e.g., mass-yield characteristics that can be directly compared with experiment. Except for a few collisions compatible with fusion or long-time quasifission, the largely dominant outcome is fast quasifission. It is shown that the orientation has also a strong influence on the scattering angle.

Fast quasifission produces peaks in the mass-yield distribution for the projectile-like and target-like fragments with a width in good agreement with empirical estimates, despite the fact that the TDHF approach does not account for beyond-mean-field fluctuations. Here, the observed fluctuations come mainly from the various orientations of the target in the entrance channel.

The influence of shell effects on the formation of the fragments has been investigated. Unlike similar reactions with ^{238}U targets, no influence of ^{208}Pb is observed unambiguously. However, elongated fragments in the ^{100}Zr region are produced in the more-peripheral quasifission reactions. More-central collisions consistently produce fragments with $N = 56$ nucleons for all orientations. This is interpreted as an effect of octupole-deformed shells favoring the production of fragments with pear shapes at scission. A similar effect has recently been discussed in the case of fission.

This is an indication of a potential influence of octupole shell gaps in quasifission. Its experimental confirmation would be particularly interesting because it would point towards strong similarities in how shell effects affect both fission and quasifission. These shell effects in the light fragments will be more easily investigated experimentally at backward angles.

ACKNOWLEDGMENTS

We thank D. J. Hinde for useful discussions. This work has been supported by the US Department of Energy under Grant No. DE-SC0013847 with Vanderbilt University and by the Australian Research Council Discovery Project (Projects No. DP160101254 and No. DP190100256) funding schemes.

[1] B. Heusch, C. Volant, H. Freiesleben, R. P. Chestnut, K. D. Hildenbrand, F. Pühlhofer, W. F. W. Schneider, B. Kohlmeyer, and W. Pfeffer, The reaction mechanism in the system ^{132}Xe + ^{56}Fe at 5.73 MeV/u: Evidence for a new type of strongly damped collisions, Z. Phys. A: At. Nucl. (1975) **288**, 391 (1978).

[2] B. B. Back, H.-G. Clerc, R. R. Betts, B. G. Glagola, and B. D. Wilkins, Observation of Anisotropy in the Fission Decay of Nuclei with Vanishing Fission Barrier, Phys. Rev. Lett. **46**, 1068 (1981).

[3] B. B. Back, R. R. Betts, K. Cassidy, B. G. Glagola, J. E. Gindler, L. E. Glendenin, and B. D. Wilkins, Experimental Signatures of Quasifission Reactions, Phys. Rev. Lett. **50**, 818 (1983).

[4] R. Bock, Y. T. Chu, M. Dakowski, A. Gobbi, E. Grosse, A. Olmi, H. Sann, D. Schwalm, U. Lynen, W. Müller, S. Bjørnholm, H. Esbensen, W. Wölfli, and E. Morenzoni, Dynamics of the fusion process, Nucl. Phys. A **388**, 334 (1982).

[5] C.-C. Sahm, H.-G. Clerc, K.-H. Schmidt, W. Reisdorf, P. Armbruster, F. P. Heßberger, J. G. Keller, G. Münzenberg, and D. Vermeulen, Hindrance of fusion in central collisions of heavy symmetric nuclear systems, Z. Phys. A: At. Nucl. (1975) **319**, 113 (1984).

[6] H. Gäggeler, T. Sikkeland, G. Wirth, W. Brüchle, W. Bögl, G. Franz, G. Herrmann, J. V. Kratz, M. Schädel, K. Sümmerer, and W. Weber, Probing sub-barrier fusion and extra-push by measuring fermium evaporation residues in different heavy ion reactions, Z. Phys. A: At. Nucl. (1975) **316**, 291 (1984).

[7] K.-H. Schmidt and W. Morawek, The conditions for the synthesis of heavy nuclei, Rep. Prog. Phys. **54**, 949 (1991).

[8] B. B. Back, H. Esbensen, C. L. Jiang, and K. E. Rehm, Recent developments in heavy-ion fusion reactions, Rev. Mod. Phys. **86**, 317 (2014).

[9] J. Khuyagbaatar, H. M. David, D. J. Hinde, I. P. Carter, K. J. Cook, M. Dasgupta, Ch. E. Düllmann, D. Y. Jeung, B. Kindler, B. Lommel, D. H. Luong, E. Prasad, D. C. Rafferty, C. Sengupta, C. Simenel, E. C. Simpson, J. F. Smith, K. Vo-Phuoc, J. Walshe, A. Wakhle, E. Williams, and A. Yakushev, Nuclear structure dependence of fusion hindrance in heavy element synthesis, Phys. Rev. C **97**, 064618 (2018).

[10] K. Banerjee, D. J. Hinde, M. Dasgupta, E. C. Simpson, D. Y. Jeung, C. Simenel, B. M. A. Swinton-Bland, E. Williams, I. P. Carter, K. J. Cook, H. M. David, C. E. Düllmann, J. Khuyagbaatar, B. Kindler, B. Lommel, E. Prasad, C. Sengupta, J. F. Smith, K. Vo-Phuoc, J. Walshe, and A. Yakushev, Mechanisms Suppressing Superheavy Element Yields in Cold Fusion Reactions, Phys. Rev. Lett. **122**, 232503 (2019).

[11] J. Tõke, R. Bock, G. X. Dai, A. Gobbi, S. Gralla, K. D. Hildenbrand, J. Kuzminski, W. F. J. Müller, A. Olmi, H. Stelzer, B. B. Back, and S. Bjørnholm, Quasi-fission: The mass-drift mode in heavy-ion reactions, Nucl. Phys. A **440**, 327 (1985).

[12] W. Q. Shen, J. Albinski, A. Gobbi, S. Gralla, K. D. Hildenbrand, N. Herrmann, J. Kuzminski, W. F. J. Müller, H. Stelzer, J. Tõke, B. B. Back, S. Bjørnholm, and S. P. Sørensen,

Fission and quasifission in U-induced reactions, Phys. Rev. C **36**, 115 (1987).

[13] R. du Rietz, D. J. Hinde, M. Dasgupta, R. G. Thomas, L. R. Gasques, M. Evers, N. Lobanov, and A. Wakhle, Predominant Time Scales in Fission Processes in Reactions of S, Ti, and Ni with W: Zeptosecond versus Attosecond, Phys. Rev. Lett. **106**, 052701 (2011).

[14] M. G. Itkis, J. Äystö, S. Beghini, A. A. Bogachev, L. Corradi, O. Dorvaux, A. Gadea, G. Giardina, F. Hanappe, I. M. Itkis, M. Jandel, J. Kliman, S. V. Khlebnikov, G. N. Kniajeva, N. A. Kondratiev, E. M. Kozulin, L. Krupa, A. Latina, T. Materna, G. Montagnoli, Yu. Ts. Oganessian, I. V. Pokrovsky, E. V. Prokhorova, N. Rowley, V. A. Rubchenya, A. Ya. Rusanov, R. N. Sagaidak, F. Scarlassara, A. M. Stefanini, L. Stuttge, S. Szilner, M. Trotta, W. H. Trzaska, D. N. Vakhtin, A. M. Vinodkumar, V. M. Voskressenski, and V. I. Zagrebaev, Shell effects in fission and quasi-fission of heavy and superheavy nuclei, Nucl. Phys. A **734**, 136 (2004).

[15] K. Nishio, H. Ikezoe, S. Mitsuoka, I. Nishinaka, Y. Nagame, Y. Watanabe, T. Ohtsuki, K. Hirose, and S. Hofmann, Effects of nuclear orientation on the mass distribution of fission fragments in the reaction of ^{36}S + ^{238}U, Phys. Rev. C **77**, 064607 (2008).

[16] E. M. Kozulin, G. N. Knyazheva, S. N. Dmitriev, I. M. Itkis, M. G. Itkis, T. A. Loktev, K. V. Novikov, A. N. Baranov, W. H. Trzaska, E. Vardaci, S. Heinz, O. Beliuskina, and S. V. Khlebnikov, Shell effects in damped collisions of ^{88}Sr with ^{176}Yb at the Coulomb barrier energy, Phys. Rev. C **89**, 014614 (2014).

[17] A. Wakhle, C. Simenel, D. J. Hinde, M. Dasgupta, M. Evers, D. H. Luong, R. du Rietz, and E. Williams, Interplay between Quantum Shells and Orientation in Quasifission, Phys. Rev. Lett. **113**, 182502 (2014).

[18] M. Morjean, D. J. Hinde, C. Simenel, D. Y. Jeung, M. Airiau, K. J. Cook, M. Dasgupta, A. Drouart, D. Jacquet, S. Kalkal, C. S. Palshetkar, E. Prasad, D. Rafferty, E. C. Simpson, L. Tassan-Got, K. Vo-Phuoc, and E. Williams, Evidence for the Role of Proton Shell Closure in Quasifission Reactions from X–Ray Fluorescence of Mass-Identified Fragments, Phys. Rev. Lett. **119**, 222502 (2017).

[19] M. Veselsky, J. Klimo, Y.-G. Ma, and G. A. Souliotis, Constraining the equation of state of nuclear matter from fusion hindrance in reactions leading to the production of superheavy elements, Phys. Rev. C **94**, 064608 (2016).

[20] H. Zheng, S. Burrello, M. Colonna, D. Lacroix, and G. Scamps, Connecting the nuclear equation of state to the interplay between fusion and quasifission processes in low-energy nuclear reactions, Phys. Rev. C **98**, 024622 (2018).

[21] B. B. Back, P. B. Fernandez, B. G. Glagola, D. Henderson, S. Kaufman, J. G. Keller, S. J. Sanders, F. Videbæk, T. F. Wang, and B. D. Wilkins, Entrance-channel effects in quasifission reactions, Phys. Rev. C **53**, 1734 (1996).

[22] K. Nishio, S. Mitsuoka, I. Nishinaka, H. Makii, Y. Wakabayashi, H. Ikezoe, K. Hirose, T. Ohtsuki, Y. Aritomo, and S. Hofmann, Fusion probabilities in the reactions ^{40,48}Ca + ^{238}U at energies around the Coulomb barrier, Phys. Rev. C **86**, 034608 (2012).

[23] E. Williams, K. Sekizawa, D. J. Hinde, C. Simenel, M. Dasgupta, I. P. Carter, K. J. Cook, D. Y. Jeung, S. D. McNeil, C. S. Palshetkar, D. C. Rafferty, K. Ramachandran, and A. Wakhle, Exploring Zeptosecond Quantum Equilibration Dynamics: From Deep-Inelastic to Fusion-Fission Outcomes in ^{58}Ni + ^{60}Ni Reactions, Phys. Rev. Lett. **120**, 022501 (2018).

[24] C. J. Lin, R. du Rietz, D. J. Hinde, M. Dasgupta, R. G. Thomas, M. L. Brown, M. Evers, L. R. Gasques, and M. D. Rodriguez, Systematic behavior of mass distributions in ^{48}Ti-induced fission at near-barrier energies, Phys. Rev. C **85**, 014611 (2012).

[25] R. du Rietz, E. Williams, D. J. Hinde, M. Dasgupta, M. Evers, C. J. Lin, D. H. Luong, C. Simenel, and A. Wakhle, Mapping quasifission characteristics and timescales in heavy element formation reactions, Phys. Rev. C **88**, 054618 (2013).

[26] D. J. Hinde, M. Dasgupta, J. R. Leigh, J. P. Lestone, J. C. Mein, C. R. Morton, J. O. Newton, and H. Timmers, Fusion-Fission versus Quasifission: Effect of Nuclear Orientation, Phys. Rev. Lett. **74**, 1295 (1995).

[27] D. J. Hinde, M. Dasgupta, J. R. Leigh, J. C. Mein, C. R. Morton, J. O. Newton, and H. Timmers, Conclusive evidence for the influence of nuclear orientation on quasifission, Phys. Rev. C **53**, 1290 (1996).

[28] G. N. Knyazheva, E. M. Kozulin, R. N. Sagaidak, A. Yu. Chizhov, M. G. Itkis, N. A. Kondratiev, V. M. Voskressensky, A. M. Stefanini, B. R. Behera, L. Corradi, E. Fioretto, A. Gadea, A. Latina, S. Szilner, M. Trotta, S. Beghini, G. Montagnoli, F. Scarlassara, F. Haas, N. Rowley, P. R. S. Gomes, and A. Szanto de Toledo, Quasifission processes in ^{40,48}Ca + ^{144,154}Sm reactions, Phys. Rev. C **75**, 064602 (2007).

[29] D. J. Hinde, R. G. Thomas, R. du Rietz, A. Diaz-Torres, M. Dasgupta, M. L. Brown, M. Evers, L. R. Gasques, R. Rafiei, and M. D. Rodriguez, Disentangling Effects of Nuclear Structure in Heavy Element Formation, Phys. Rev. Lett. **100**, 202701 (2008).

[30] C. Simenel, D. J. Hinde, R. du Rietz, M. Dasgupta, M. Evers, C. J. Lin, D. H. Luong, and A. Wakhle, Influence of entrance-channel magicity and isospin on quasi-fission, Phys. Lett. B **710**, 607 (2012).

[31] G. Mohanto, D. J. Hinde, K. Banerjee, M. Dasgupta, D. Y. Jeung, C. Simenel, E. C. Simpson, A. Wakhle, E. Williams, I. P. Carter, K. J. Cook, D. H. Luong, C. S. Palshetkar, and D. C. Rafferty, Interplay of spherical closed shells and N/Z asymmetry in quasifission dynamics, Phys. Rev. C **97**, 054603 (2018).

[32] K. Hammerton, Z. Kohley, D. J. Hinde, M. Dasgupta, A. Wakhle, E. Williams, V. E. Oberacker, A. S. Umar, I. P. Carter, K. J. Cook, J. Greene, D. Y. Jeung, D. H. Luong, S. D. McNeil, C. S. Palshetkar, D. C. Rafferty, C. Simenel, and K. Stiefel, Reduced quasifission competition in fusion reactions forming neutron-rich heavy elements, Phys. Rev. C **91**, 041602(R) (2015).

[33] K. Hammerton, D. J. Morrissey, Z. Kohley, D. J. Hinde, M. Dasgupta, A. Wakhle, E. Williams, I. P. Carter, K. J. Cook, J. Greene, D. Y. Jeung, D. H. Luong, S. D. McNeil, C. Palshetkar, D. C. Rafferty, C. Simenel, and K. Stiefel, Entrance channel effects on the quasifission reaction channel in Cr + W systems, Phys. Rev. C **99**, 054621 (2019).

[34] A. Diaz-Torres, G. G. Adamian, N. V. Antonenko, and W. Scheid, Quasifission process in a transport model for a dinuclear system, Phys. Rev. C **64**, 024604 (2001).

[35] G. G. Adamian, N. V. Antonenko, and W. Scheid, Characteristics of quasifission products within the dinuclear system model, Phys. Rev. C **68**, 034601 (2003).

[36] M. Huang, Z. Gan, X. Zhou, J. Li, and W. Scheid, Competing fusion and quasifission reaction mechanisms in the production of superheavy nuclei, Phys. Rev. C **82**, 044614 (2010).

[37] X. J. Bao, Y. Gao, J. Q. Li, and H. F. Zhang, Theoretical study of the synthesis of superheavy nuclei using radioactive beams, Phys. Rev. C **91**, 064612 (2015).

[38] S. Q. Guo, Y. Gao, J. Q. Li, and H. F. Zhang, Dynamical deformation in heavy ion reactions and the characteristics of quasifission products, Phys. Rev. C **96**, 044622 (2017).

[39] V. Zagrebaev and W. Greiner, Unified consideration of deep inelastic, quasi-fission and fusion-fission phenomena, J. Phys. G **31**, 825 (2005).

[40] Y. Aritomo, Analysis of dynamical processes using the mass distribution of fission fragments in heavy-ion reactions, Phys. Rev. C **80**, 064604 (2009).

[41] Y. Aritomo, K. Hagino, K. Nishio, and S. Chiba, Dynamical approach to heavy-ion induced fission using actinide target nuclei at energies around the Coulomb barrier, Phys. Rev. C **85**, 044614 (2012).

[42] A. V. Karpov and V. V. Saiko, Modeling near-barrier collisions of heavy ions based on a Langevin-type approach, Phys. Rev. C **96**, 024618 (2017).

[43] K. Sekizawa and K. Hagino, Time-dependent Hartree-Fock plus Langevin approach for hot fusion reactions to synthesize the $Z = 120$ superheavy element, Phys. Rev. C **99**, 051602 (2019).

[44] K. Wen, F. Sakata, Z.-X. Li, X.-Z. Wu, Y.-X. Zhang, and S.-G. Zhou, Non-Gaussian Fluctuations and Non-Markovian Effects in the Nuclear Fusion Process: Langevin Dynamics Emerging from Quantum Molecular Dynamics Simulations, Phys. Rev. Lett. **111**, 012501 (2013).

[45] N. Wang and L. Guo, New neutron-rich isotope production in ^{154}Sm + ^{160}Gd, Phys. Lett. B **760**, 236 (2016).

[46] K. Zhao, Z. Li, Y. Zhang, N. Wang, Q. Li, C. Shen, Y. Wang, and X. Wu, Production of unknown neutron–rich isotopes in ^{238}U + ^{238}U collisions at near-barrier energy, Phys. Rev. C **94**, 024601 (2016).

[47] C. Golabek and C. Simenel, Collision Dynamics of Two ^{238}U Atomic Nuclei, Phys. Rev. Lett. **103**, 042701 (2009).

[48] D. J. Kedziora and C. Simenel, New inverse quasifission mechanism to produce neutron-rich transfermium nuclei, Phys. Rev. C **81**, 044613 (2010).

[49] V. E. Oberacker, A. S. Umar, and C. Simenel, Dissipative dynamics in quasifission, Phys. Rev. C **90**, 054605 (2014).

[50] A. S. Umar, V. E. Oberacker, and C. Simenel, Shape evolution and collective dynamics of quasifission in the time-dependent Hartree-Fock approach, Phys. Rev. C **92**, 024621 (2015).

[51] A. S. Umar, V. E. Oberacker, and C. Simenel, Fusion and quasifission dynamics in the reactions ^{48}Ca + ^{249}Bk and ^{50}Ti + ^{249}Bk using a time-dependent Hartree-Fock approach, Phys. Rev. C **94**, 024605 (2016).

[52] K. Sekizawa and K. Yabana, Time-dependent Hartree-Fock calculations for multinucleon transfer and quasifission processes in the ^{64}Ni + ^{238}U reaction, Phys. Rev. C **93**, 054616 (2016).

[53] C. Yu and L. Guo, Angular momentum dependence of quasifission dynamics in the reaction ^{48}Ca + ^{244}Pu, Sci. China: Phys., Mech. Astron. **60**, 092011 (2017).

[54] S. Ayik, B. Yilmaz, O. Yilmaz, A. S. Umar, and G. Turan, Multinucleon transfer in central collisions of ^{238}U + ^{238}U, Phys. Rev. C **96**, 024611 (2017).

[55] S. Ayik, B. Yilmaz, O. Yilmaz, and A. S. Umar, Quantal diffusion description of multinucleon transfers in heavy-ion collisions, Phys. Rev. C **97**, 054618 (2018).

[56] K. Sekizawa, Enhanced nucleon transfer in tip collisions of ^{238}U + ^{124}Sn, Phys. Rev. C **96**, 041601(R) (2017).

[57] A. Wakhle, K. Hammerton, Z. Kohley, D. J. Morrissey, K. Stiefel, J. Yurkon, J. Walshe, K. J. Cook, M. Dasgupta, D. J. Hinde, D. J. Jeung, E. Prasad, D. C. Rafferty, C. Simenel, E. C. Simpson, K. Vo-Phuoc, J. King, W. Loveland, and R. Yanez, Capture cross sections for the synthesis of new heavy nuclei using radioactive beams, Phys. Rev. C **97**, 021602 (2018).

[58] C. Simenel, Nuclear quantum many-body dynamics, Eur. Phys. J. A **48**, 152 (2012).

[59] C. Simenel and A. S. Umar, Heavy-ion collisions and fission dynamics with the time-dependent Hartree-Fock theory and its extensions, Prog. Part. Nucl. Phys. **103**, 19 (2018).

[60] K. Sekizawa, TDHF theory and its extensions for the multinucleon transfer reaction: A mini review, Front. Phys. **7**, 20 (2019).

[61] P. D. Stevenson and M. C. Barton, Low–energy heavy-ion reactions and the Skyrme effective interaction, Prog. Part. Nucl. Phys. **104**, 142 (2019).

[62] G. Scamps and C. Simenel, Impact of pear-shaped fission fragments on mass-asymmetric fission in actinides, Nature (London) **564**, 382 (2018).

[63] G. Scamps and C. Simenel, Effect of shell structure on the fission of sub-lead nuclei, arXiv:1904.01275.

[64] D. N. Poenaru and R. A. Gherghescu, α decay and cluster radioactivity of nuclei of interest to the synthesis of $Z = 119$, 120 isotopes, Phys. Rev. C **97**, 044621 (2018).

[65] M. Warda, A. Zdeb, and L. M. Robledo, Cluster radioactivity in superheavy nuclei, Phys. Rev. C **98**, 041602 (2018).

[66] Z. Matheson, S. A. Giuliani, W. Nazarewicz, J. Sadhukhan, and N. Schunck, Cluster radioactivity of $^{294}_{118}$Og$_{176}$, Phys. Rev. C **99**, 041304 (2019).

[67] Y. L. Zhang and Y. Z. Wang, Systematic study of cluster radioactivity of superheavy nuclei, Phys. Rev. C **97**, 014318 (2018).

[68] Yu. Ts. Oganessian, F. Sh. Abdullin, P. D. Bailey, D. E. Benker, M. E. Bennett, S. N. Dmitriev, J. G. Ezold, J. H. Hamilton, R. A. Henderson, M. G. Itkis, Yu. V. Lobanov, A. N. Mezentsev, K. J. Moody, S. L. Nelson, A. N. Polyakov, C. E. Porter, A. V. Ramayya, F. D. Riley, J. B. Roberto, M. A. Ryabinin, K. P. Rykaczewski, R. N. Sagaidak, D. A. Shaughnessy, I. V. Shirokovsky, M. A. Stoyer, V. G. Subbotin, R. Sudowe, A. M. Sukhov, Yu. S. Tsyganov, V. K. Utyonkov, A. A. Voinov, G. K. Vostokin, and P. A. Wilk, Synthesis of a New Element with Atomic Number $Z = 117$, Phys. Rev. Lett. **104**, 142502 (2010).

[69] Yu. Ts. Oganessian, F. Sh. Abdullin, P. D. Bailey, D. E. Benker, M. E. Bennett, S. N. Dmitriev, J. G. Ezold, J. H. Hamilton, R. A. Henderson, M. G. Itkis, Yu. V. Lobanov, A. N. Mezentsev, K. J. Moody, S. L. Nelson, A. N. Polyakov, C. E. Porter, A. V. Ramayya, F. D. Riley, J. B. Roberto, M. A. Ryabinin, K. P. Rykaczewski, R. N. Sagaidak, D. A. Shaughnessy, I. V. Shirokovsky, M. A. Stoyer, V. G. Subbotin, R. Sudowe, A. M. Sukhov, R. Taylor, Yu. S. Tsyganov, V. K. Utyonkov, A. A. Voinov, G. K. Vostokin, and P. A. Wilk, Eleven new heaviest isotopes of elements $Z = 105$ to $Z = 117$ identified among the products of ^{249}Bk + ^{48}Ca reactions, Phys. Rev. C **83**, 054315 (2011).

[70] Yu. Ts. Oganessian, F. Sh. Abdullin, C. Alexander, J. Binder, R. A. Boll, S. N. Dmitriev, J. Ezold, K. Felker, J. M. Gostic, R. K. Grzywacz, J. H. Hamilton, R. A. Henderson, M. G. Itkis, K. Miernik, D. Miller, K. J. Moody, A. N. Polyakov, A. V. Ramayya, J. B. Roberto, M. A. Ryabinin, K. P. Rykaczewski, R. N. Sagaidak, D. A. Shaughnessy, I. V. Shirokovsky, M. V. Shumeiko, M. A. Stoyer, N. J. Stoyer, V. G. Subbotin, A. M. Sukhov, Yu. S.. Tsyganov, V. K. Utyonkov, A. A. Voinov, and G. K. Vostokin, Production and Decay of the Heaviest Nuclei ^{293,294}117 and ^{294}118, Phys. Rev. Lett. **109**, 162501 (2012).

[71] Yu. Ts. Oganessian, F. Sh. Abdullin, C. Alexander, J. Binder, R. A. Boll, S. N. Dmitriev, J. Ezold, K. Felker, J. M. Gostic, R. K. Grzywacz, J. H. Hamilton, R. A. Henderson, M. G. Itkis, K. Miernik, D. Miller, K. J. Moody, A. N. Polyakov, A. V. Ramayya, J. B. Roberto, M. A. Ryabinin, K. P. Rykaczewski, R. N. Sagaidak, D. A. Shaughnessy, I. V. Shirokovsky, M. V. Shumeiko, M. A. Stoyer, N. J. Stoyer, V. G. Subbotin, A. M. Sukhov, Yu. S.. Tsyganov, V. K. Utyonkov, A. A. Voinov, and G. K. Vostokin, Experimental studies of the ^{249}Bk + ^{48}Ca reaction including decay properties and excitation function for isotopes of element 117, and discovery of the new isotope ^{277}Mt, Phys. Rev. C **87**, 054621 (2013).

[72] J. Khuyagbaatar, A. Yakushev, Ch. E. Düllmann, D. Ackermann, L.-L. Andersson, M. Asai, M. Block, R. A. Boll, H. Brand, D. M. Cox, M. Dasgupta, X. Derkx, A. Di Nitto, K. Eberhardt, J. Even, M. Evers, C. Fahlander, U. Forsberg, J. M. Gates, N. Gharibyan, P. Golubev, K. E. Gregorich, J. H. Hamilton, W. Hartmann, R.-D. Herzberg, F. P. Heßberger, D. J. Hinde, J. Hoffmann, R. Hollinger, A. Hübner, E. Jäger, B. Kindler, J. V. Kratz, J. Krier, N. Kurz, M. Laatiaoui, S. Lahiri, R. Lang, B. Lommel, M. Maiti, K. Miernik, S. Minami, A. Mistry, C. Mokry, H. Nitsche, J. P. Omtvedt, G. K. Pang, P. Papadakis, D. Renisch, J. Roberto, D. Rudolph, J. Runke, K. P. Rykaczewski, L. G. Sarmiento, M. Schädel, B. Schausten, A. Semchenkov, D. A. Shaughnessy, P. Steinegger, J. Steiner, E. E. Tereshatov, P. Thörle-Pospiech, K. Tinschert, T. Torres De Heidenreich, N. Trautmann, A. Türler, J. Uusitalo, D. E. Ward, M. Wegrzecki, N. Wiehl, S. M. Van Cleve, and V. Yakusheva, ^{48}Ca + ^{249}Bk Fusion Reaction Leading to Element $Z = 117$: Long-Lived α-Decaying ^{270}Db and Discovery of ^{266}Lr, Phys. Rev. Lett. **112**, 172501 (2014).

[73] J. W. Negele, The mean-field theory of nuclear-structure and dynamics, Rev. Mod. Phys. **54**, 913 (1982).

[74] P. Bonche, B. Grammaticos, and S. Koonin, Three-dimensional time-dependent Hartree-Fock calculations of ^{16}O + ^{16}O and ^{40}Ca + ^{40}Ca fusion cross sections, Phys. Rev. C **17**, 1700 (1978).

[75] H. Flocard, S. E. Koonin, and M. S. Weiss, Three-dimensional time-dependent Hartree-Fock calculations: Application to ^{16}O + ^{16}O collisions, Phys. Rev. C **17**, 1682 (1978).

[76] C. Simenel, P. Chomaz, and G. de France, Quantum Calculation of the Dipole Excitation in Fusion Reactions, Phys. Rev. Lett. **86**, 2971 (2001).

[77] A. S. Umar, V. E. Oberacker, and J. A. Maruhn, Neutron transfer dynamics and doorway to fusion in time-dependent Hartree-Fock theory, Eur. Phys. J. A **37**, 245 (2008).

[78] A. S. Umar and V. E. Oberacker, Time dependent Hartree-Fock fusion calculations for spherical, deformed systems, Phys. Rev. C **74**, 024606 (2006).

[79] K. Washiyama and D. Lacroix, Energy dependence of the nucleus-nucleus potential close to the Coulomb barrier, Phys. Rev. C **78**, 024610 (2008).

[80] A. S. Umar, V. E. Oberacker, J. A. Maruhn, and P.-G. Reinhard, Entrance channel dynamics of hot and cold fusion reactions leading to superheavy elements, Phys. Rev. C **81**, 064607 (2010).

[81] L. Guo and T. Nakatsukasa, Time-dependent Hartree-Fock studies of the dynamical fusion threshold, EPJ Web Conf. **38**, 09003 (2012).

[82] R. Keser, A. S. Umar, and V. E. Oberacker, Microscopic study of Ca+ Ca fusion, Phys. Rev. C **85**, 044606 (2012).

[83] C. Simenel, R. Keser, A. S. Umar, and V. E. Oberacker, Microscopic study of ^{16}O + ^{16}O fusion, Phys. Rev. C **88**, 024617 (2013).

[84] V. E. Oberacker, A. S. Umar, J. A. Maruhn, and P.-G. Reinhard, Dynamic microscopic study of pre-equilibrium giant resonance excitation and fusion in the reactions ^{132}Sn + ^{48}Ca and ^{124}Sn + ^{40}Ca, Phys. Rev. C **85**, 034609 (2012).

[85] V. E. Oberacker, A. S. Umar, J. A. Maruhn, and P. G. Reinhard, Microscopic study of the ^{132,124}Sn + ^{96}Zr reactions: Dynamic excitation energy, energy-dependent heavy-ion potential, and capture cross section, Phys. Rev. C **82**, 034603 (2010).

[86] A. S. Umar, V. E. Oberacker, and C. J. Horowitz, Microscopic sub-barrier fusion calculations for the neutron star crust, Phys. Rev. C **85**, 055801 (2012).

[87] C. Simenel, M. Dasgupta, D. J. Hinde, and E. Williams, Microscopic approach to coupled-channels effects on fusion, Phys. Rev. C **88**, 064604 (2013).

[88] A. S. Umar, C. Simenel, and V. E. Oberacker, Energy dependence of potential barriers and its effect on fusion cross sections, Phys. Rev. C **89**, 034611 (2014).

[89] X. Jiang, J. A. Maruhn, and S. Yan, Microscopic study of noncentral effects in heavy-ion fusion reactions with spherical nuclei, Phys. Rev. C **90**, 064618 (2014).

[90] S. E. Koonin, K. T. R. Davies, V. Maruhn-Rezwani, H. Feldmeier, S. J. Krieger, and J. W. Negele, Time-dependent Hartree-Fock calculations for ^{16}O + ^{16}O and ^{40}Ca + ^{40}Ca reactions, Phys. Rev. C **15**, 1359 (1977).

[91] C. Simenel, Particle Transfer Reactions with the Time-Dependent Hartree-Fock Theory Using a Particle Number Projection Technique, Phys. Rev. Lett. **105**, 192701 (2010).

[92] C. Simenel, Particle-Number Fluctuations and Correlations in Transfer Reactions Obtained Using the Balian-Vénéroni Variational Principle, Phys. Rev. Lett. **106**, 112502 (2011).

[93] K. Sekizawa and K. Yabana, Time-dependent Hartree-Fock calculations for multinucleon transfer processes in ^{40,48}Ca + ^{124}Sn, ^{40}Ca + ^{208}Pb, and ^{58}Ni + ^{208}Pb reactions, Phys. Rev. C **88**, 014614 (2013).

[94] G. Scamps and D. Lacroix, Effect of pairing on one- and two-nucleon transfer below the Coulomb barrier: A time-dependent microscopic description, Phys. Rev. C **87**, 014605 (2013).

[95] K. Sekizawa and K. Yabana, Particle-number projection method in time-dependent Hartree-Fock theory: Properties of reaction products, Phys. Rev. C **90**, 064614 (2014).

[96] D. Bourgin, C. Simenel, S. Courtin, and F. Haas, Microscopic study of ^{40}Ca + ^{58,64}Ni fusion reactions, Phys. Rev. C **93**, 034604 (2016).

[97] A. S. Umar, C. Simenel, and W. Ye, Transport properties of isospin asymmetric nuclear matter using the time-dependent Hartree-Fock method, Phys. Rev. C **96**, 024625 (2017).
[98] C. Simenel and A. S. Umar, Formation and dynamics of fission fragments, Phys. Rev. C **89**, 031601(R) (2014).
[99] A. S. Umar and V. E. Oberacker, Time-dependent HF approach to SHE dynamics, Nucl. Phys. A **944**, 238 (2015).
[100] G. Scamps, C. Simenel, and D. Lacroix, Superfluid dynamics of ^{258}Fm fission, Phys. Rev. C **92**, 011602 (2015).
[101] P. M. Goddard, P. D. Stevenson, and A. Rios, Fission dynamics within time-dependent Hartree-Fock: Deformation-induced fission, Phys. Rev. C **92**, 054610 (2015).
[102] A. Bulgac, P. Magierski, K. J. Roche, and I. Stetcu, Induced Fission of ^{240}Pu within a Real-Time Microscopic Framework, Phys. Rev. Lett. **116**, 122504 (2016).
[103] C. Bottcher, M. R. Strayer, A. S. Umar, and P.-G. Reinhard, Damped relaxation techniques to calculate relativistic bound states, Phys. Rev. A **40**, 4182 (1989).
[104] A. S. Umar and V. E. Oberacker, Three-dimensional unrestricted time-dependent Hartree-Fock fusion calculations using the full Skyrme interaction, Phys. Rev. C **73**, 054607 (2006).
[105] J. A. Maruhn, P.-G. Reinhard, P. D. Stevenson, and A. S. Umar, The TDHF Code Sky3D, Comput. Phys. Commun. **185**, 2195 (2014).
[106] K.–H. Kim, T. Otsuka, and P. Bonche, Three-dimensional TDHF calculations for reactions of unstable nuclei, J. Phys. G **23**, 1267 (1997).
[107] D. A. Pigg, A. S. Umar, and V. E. Oberacker, Eulerian rotations of deformed nuclei for TDDFT calculations, Comput. Phys. Commun. **185**, 1410 (2014).
[108] V. E. Viola, K. Kwiatkowski, and M. Walker, Systematics of fission fragment total kinetic-energy release, Phys. Rev. C **31**, 1550 (1985).
[109] D. J. Hinde, J. R. Leigh, J. J. M. Bokhorst, J. O. Newton, R. L. Walsh, and J. W. Boldeman, Mass-split dependence of the pre- and post-scission neutron multiplicities for fission of ^{251}Es, Nucl. Phys. A **472**, 318 (1987).
[110] D. J. Hinde, D. Y. Jeung, E. Prasad, A. Wakhle, M. Dasgupta, M. Evers, D. H. Luong, R. du Rietz, C. Simenel, E. C. Simpson, and E. Williams, Sub–barrier quasifission in heavy element formation reactions with deformed actinide target nuclei, Phys. Rev. C **97**, 024616 (2018).
[111] G. Scamps and Y. Hashimoto, Transfer probabilities for the reactions ^{14,20}O + ^{20}O in terms of multiple time-dependent Hartree-Fock-Bogoliubov trajectories, Phys. Rev. C **96**, 031602 (2017).
[112] C. H. Dasso, T. Dossing, and H. C. Pauli, On the mass distribution in time-dependent Hartree-Fock calculations of heavy-ion collisions, Z. Phys. A: At. Nucl. (1975) **289**, 395 (1979).
[113] D. Lacroix and S. Ayik, Stochastic quantum dynamics beyond mean field, Eur. Phys. J. A **50**, 95 (2014).
[114] S. Ayik, O. Yilmaz, B. Yilmaz, A. S. Umar, A. Gokalp, G. Turan, and D. Lacroix, Quantal description of nucleon exchange in a stochastic mean-field approach, Phys. Rev. C **91**, 054601 (2015).
[115] S. Ayik, B. Yilmaz, and O. Yilmaz, Multinucleon exchange in quasifission reactions, Phys. Rev. C **92**, 064615 (2015).
[116] S. Ayik, O. Yilmaz, B. Yilmaz, and A. S. Umar, Quantal nucleon diffusion: Central collisions of symmetric nuclei, Phys. Rev. C **94**, 044624 (2016).
[117] Y. Tanimura, D. Lacroix, and S. Ayik, Microscopic Phase-Space Exploration Modeling of ^{258}Fm Spontaneous Fission, Phys. Rev. Lett. **118**, 152501 (2017).
[118] G. A. Lalazissis, S. Raman, and P. Ring, Ground–state properties of even-even nuclei in the relativistic mean-field theory, At. Data Nucl. Data Tables **71**, 1 (1999).
[119] A. Blazkiewicz, V. E. Oberacker, A. S. Umar, and M. Stoitsov, Coordinate space Hartree-Fock-Bogoliubov calculations for the zirconium isotope chain up to the two-neutron drip line, Phys. Rev. C **71**, 054321 (2005).
[120] J. K. Hwang, A. V. Ramayya, J. H. Hamilton, Y. X. Luo, A. V. Daniel, G. M. Ter-Akopian, J. D. Cole, and S. J. Zhu, Half-life measurements of several states in ^{95,97}Sr, ^{97,100,104}Zr, ^{106}Mo, and ^{148}Ce, Phys. Rev. C **73**, 044316 (2006).